

# Scaling of highly excited Schrödinger-Poisson eigenstates and universality of their rotation curves

Gaia Marangon<sup>a,\*</sup>, Antonio Ponso<sup>a,b</sup>, Lorenzo Zanelli<sup>a,b</sup>

<sup>a</sup>Department of Mathematics “Tullio Levi-Civita”, University of Padova, Via Trieste, 63, Padova, 35121, Italy

<sup>b</sup>Padua Quantum Technologies Research Center (QTech), Via Gradenigo, 6/A, Padova, 35121, Italy

## Abstract

This work provides a comprehensive numerical characterization of the excited spherically symmetric stationary states of the Schrödinger-Poisson problem. The analysis is conducted with reference to dark matter distributions around galaxies; the squared modulus of the eigenfunction represents the dark matter density distribution, and an associated eigenvelocity models the experimental galactic rotation curves. This paper aims to establish a connection between the fundamental structure of these eigenfunctions and eigenvelocities and the physical properties of the system.

Through numerical simulations of highly excited eigenstates, novel heuristic laws are proposed, which describe how their fundamental features scale with the excitation index  $n$ . Key characteristics of the eigenfunctions include: the effective support, which exhibits a parabolic dependence on the excitation index; the distances between adjacent nodes, whose pattern varies regularly with  $n$ ; and the oscillation amplitude, which follows a power law with an exponent approaching  $-1$  for large  $n$ , consistent with astrophysical observations. The eigenvelocities exhibit a mid-range oscillatory region with an average linear trend, whose slope approaches zero in the large  $n$  limit, consistent with the physical expectation of a flat plateau for the rotation curves. Additionally, we derive heuristic scaling relationships with the excitation index  $n$ , revealing a *universal behavior* in the predicted rotation curves.

**Keywords:** Schrödinger-Poisson, Scaling, Excited stationary states, Rotation curves, Universality, Plateau

## 1. Introduction

The Schrödinger-Poisson model is currently the leading description of dark matter distributions around galaxies [1, 2]. Based on the assumption of ultralight particles [2, 3, 4, 5, 6], it describes the evolution of a matter field  $\psi(t, x)$  via the Schrödinger equation, where  $|\psi|^2(t, x)$  represents the dark matter particle density distribution. The particles are subjected to self-gravity, which is modeled through a Poisson potential  $\phi(t, x)$ , with the particle density  $|\psi|^2(t, x)$  acting as the source. In dimensionless form, the system reads:

$$\begin{cases} i\partial_t \psi(t, x) = (-\Delta + 2\phi(t, x))\psi(t, x) \\ \Delta\phi(t, x) = |\psi|^2(t, x) \end{cases} \quad \text{with } x \in \mathbb{R}^3. \quad (1)$$

Current dark matter distributions are generally considered to have reached a stationary state. Consequently, they are typically modeled using the Schrödinger-Poisson stationary states (see [3, 5]) – solutions to system (1) of the form  $(e^{i\epsilon t} f(x), \phi(x))$ . The state-of-the-art primarily focuses on radially symmetric stationary states, which comprise an infinite, discrete family  $\{\epsilon_n, f_n(r), \phi_n(r)\}_{n=0}^{\infty}$ , with positive eigenvalues  $\epsilon_n > 0$ , real eigenfunctions  $f_n(r)$  and excitation index  $n \in \mathbb{N}$  (see [7]). As

suggested by Sin [5], and as shown in Figure 1, the  $n$ -th excited stationary state represents dark matter distributions as  $n+1$  concentric shells, separated by voids and exhibiting decreasing density outwards. A rigorous characterization of this structure and its dependence on the excitation index  $n$  remains incomplete, which this paper aims to address.

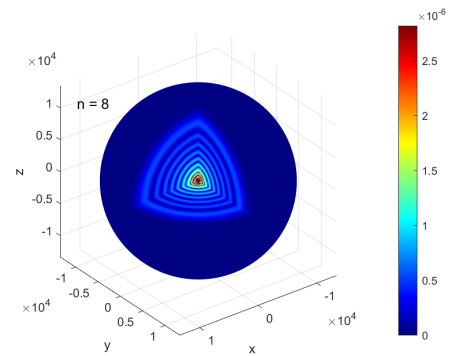


Figure 1: Three-dimensional section of the dark matter distribution, as predicted by the 8-th stationary state  $f_8(r)$ . For visualization purposes, the modulus  $|f_8(r)|$  is shown rather than the actual predicted matter density  $|f_8|^2(r)$ . The structure exhibits 9 shells of decreasing density separated by 8 voids (shown in dark blue).

Given a predicted dark matter distribution  $f_n^2(r)$ , one can calculate the tangential velocity of a test object in circular orbit at radius  $r$  from the distribution’s center. This calculation assumes

\*Corresponding author.

Email addresses: marangon@math.unipd.it (Gaia Marangon), ponso@math.unipd.it (Antonio Ponso), lzanelli@math.unipd.it (Lorenzo Zanelli)

the velocity is determined by the gravitational force exerted by matter within a sphere of radius  $r$  (see Sin [5]):

$$v_n(r) = \sqrt{\frac{\int_0^r f_n^2(s)s^2 ds}{r}}. \quad (2)$$

This prediction plays a crucial role, as it can be compared with experimental rotation curves of spiral galaxies [8, 9, 10, 11, 12], providing both model validation and deeper physical insights into the problem. Thus, we aim to provide a comprehensive, quantitative description of the eigenvelocities (2) arising from the Schrödinger-Poisson model, characterizing their key features and relating them to established physical expectations.

### 1.1. Comparison with previous works and main results

From an analytical perspective, pioneering work on Schrödinger-Poisson stationary states was conducted by Lieb [13], who established the well-posedness of the ground state, and Lions [7], who first described excited stationary states. Numerical investigations of low-excitation states ( $n \lesssim 15$ ) were later performed by Bernstein et al. [14], Moroz et al. [15], Harrison et al. [16], providing significant qualitative insights into eigenfunction properties. These eigenfunctions display oscillatory behavior, featuring  $n$  nodes and  $n + 1$  local extrema of alternating sign with diminishing amplitudes, decaying monotonically to zero beyond the last oscillation. To address the lack of exact analytical expressions, alternative density functions such as  $\rho(r) = \sin(r)r^{-1}$  were proposed (see [1, 17]). While these approximations are widely adopted in physical applications, they are inadequate to capture both the irregular nodal spacing and the precise power law decay of the eigenfunctions, highlighting the need for deeper structural understanding.

Subsequent work provided partial analytical support for these numerical observations. Tod and Moroz [18] demonstrated the smoothness and boundedness of the eigenfunctions, while Tod [19], focused on bounds, proving that all eigenvalues are negative. Greiner and Wunner [20] established connections with quantum defect theory, and Kiessling [21] investigated the long-range behavior of the eigenfunctions.

However, a comprehensive analysis of how properties scale with the excitation index  $n$  remains lacking. To address this gap, we propose quantitative, heuristic laws derived from numerical simulations of highly excited stationary states ( $n \leq 80$ ), aiming to provide foundations for future analytical and physical studies. Specifically, we analyze the eigenfunctions' structure, characterizing them as oscillatory functions modulated by a power law. The radial position of the last oscillation, which approximately defines the eigenfunction support, exhibits a clear parabolic dependence on  $n$ , characteristic of Keplerian problems like the Bohr model for the hydrogen atom (see e.g. [22]). The spacing between adjacent nodes increases with the radial position, following a consistent pattern across increasing  $n$  values – showing modest increases at small radii and more pronounced increases at larger radii. This behavior constitutes a key correction to the  $\sin(r)r^{-1}$  approximation, which fails to account for irregular nodal spacing. Finally, the power law governing amplitude modulation is characterized by

fitting local extrema at small radial positions, with deviations observed near the last extremum. The power law exponent approaches  $-1$  asymptotically as  $n$  increases, recovering the  $r^{-1}$  approximation in the large  $n$  limit.

From a physical perspective, rotation curves serve as the primary experimental reference for comparing with analytical predictions. Observed rotation curves typically show mid-range oscillatory behavior with an approximately linear trend, forming a plateau. This plateau generally exhibits a near-flat slope, though both positive and negative slopes have also been documented (see e.g. [23, 24, 8]). Moreover, physical intuition suggests that galactic-scale dark matter clusters, which generate these rotation curves, might exhibit some kind of universal behavior, as first noted by Rubin et al. [25], Burstein and Rubin [26].

The numerical results presented in this paper align well with these physical observations. In particular, the large- $n$  approximation  $f_n(r) \sim r^{-1}$ , derived from the local extrema fit, suggests that the corresponding eigenvelocity (2) remains approximately constant, consistent with an expected flat plateau. Finally, we find that the velocity at the last local oscillation exhibits a clear dependence on its radial position, which itself varies with  $n$ . This relationship reveals appropriate scaling laws under which all predicted eigenvelocities converge to a similar shape, independent of  $n$ , exhibiting some kind of universal behavior in the predicted rotation curves and confirming that our model effectively captures expected physical properties.

## 2. Model

The Schrödinger-Poisson model (1) describes the dynamics of a particle density  $|\psi|^2(t, x)$  under self-gravity. The model couples a Schrödinger equation for the matter field  $\psi(t, x)$  with a Poisson equation for the potential  $\phi(t, x)$ . Its stationary states are expressed in the form  $(e^{i\epsilon t} f(x), \phi(x))$ , where the phase oscillation in time naturally emerges from the norm conservation law  $\partial_t (\int_{\mathbb{R}^3} |\psi(t, x)|^2 d^3x) = 0$ , with  $\epsilon$  representing the associated energy parameter. The spatial component  $f(x)$  of the matter field can be assumed real without loss of generality.

As noted by Lieb [13], the problem exhibits invariance under norm scaling:

$$\tilde{x} = N^{-1}x; \quad \tilde{t} = N^{-1}t; \quad \tilde{f} = N^2 f; \quad \tilde{\phi} = N^2 \phi. \quad (3)$$

This introduces a degree of freedom in defining stationary states, which is resolved by selecting a specific value for the  $L^2(\mathbb{R}^3)$ -norm of  $f$ . Including this normalization constraint and explicitly solving the Poisson equation, the stationary problem becomes:

$$\begin{cases} \Delta f(x) + \frac{1}{2\pi} \left( \int_{\mathbb{R}^3} \frac{f^2(y)}{|x-y|} d^3y \right) f(x) = \epsilon f(x) & (4a) \\ \phi(x) = -\frac{1}{4\pi} \int_{\mathbb{R}^3} \frac{f^2(y)}{|x-y|} d^3y & (4b) \\ \int f^2(x) d^3x = 1 & (4c) \end{cases}$$

where equation (4a) is known as the Choquard equation and represents a nonlinear eigenvalue problem, with eigenvalue  $\varepsilon$  and eigenfunction  $f(x)$ . Following the prevailing approach in the literature, we focus on spherically symmetric solutions<sup>1</sup>, which form an infinite, discrete family  $\{\varepsilon_n, f_n(r), \phi_n(r)\}_{n=0}^{\infty}$ , with excitation index  $n \in \mathbb{N}$  (see Lions [7]). For each eigenfunction  $f_n(r)$ , we associate the velocity field  $v_n(r)$  defined in (2), that represents the analytical counterpart of experimental rotation curves (in the definition, we omit the factor  $4\pi$  from angular integration for simplicity).

### 2.1. Implementation

Eigenstates  $\{\varepsilon_n, f_n(r), \phi_n(r), v_n(r)\}_{n=0}^{\infty}$  are numerically simulated up to high excitation indices ( $n \leq 80$ ) following the implementation described by Bernstein et al. [14] (see also [16]). The numerical scheme employs two nested iterative procedures: an outer iteration handles the representation of the infinite domain, while an inner iteration solves problem (4) on a fixed domain. Specifically, the outer iterative procedure progressively extends the computational domain until the eigenvalue correction falls below a specific tolerance. The inner procedure decouples problem (4) by using previous-step approximations (or an initial guess for the first step) for the unknowns  $f(r)$  and  $\phi(r)$ , solving the resulting approximate problem to achieve increasingly accurate solutions.

To verify algorithmic robustness, simulations were performed with various spatial grid refinements. This validation process allowed to monitor the quality of the results, confirming reliability up to  $n = 80$ , while results for higher excitation indices were deemed insufficiently accurate for this study and excluded from the analysis.

## 3. Heuristic Laws

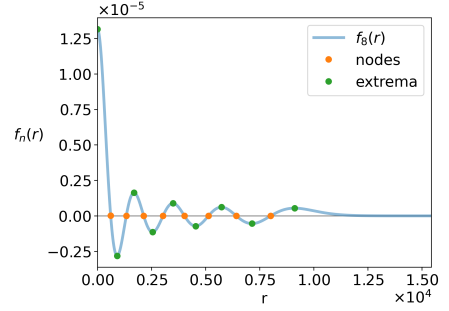
The numerical implementation of excited stationary states enables a comprehensive quantitative analysis of their structure. We first present their qualitative characteristics, identifying key features and establishing notation. Then, we conduct a systematic study, deriving heuristic laws that describe how fundamental properties scale with the excitation index  $n$ .

### 3.1. Eigenfunctions: main features and notation

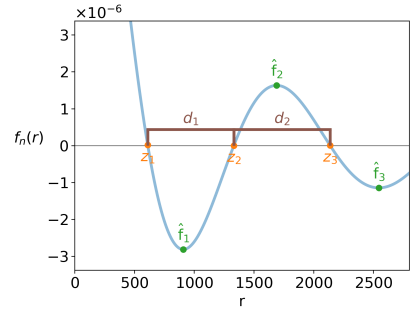
The structure of the  $n$ -th eigenfunction  $f_n(r)$  is illustrated in Figure 2, which states the notation for its key features. For clarity, the figure shows an eigenfunction with a low excitation index ( $n = 8$ ), though the structure remains analogous for highly excited eigenstates.

The function exhibits an oscillatory behavior with  $n$  nodes and  $n + 1$  local extrema. The nodes are defined as the  $n$  radial positions  $\{z_i\}_{i=1}^n$  where the eigenfunction vanishes,  $f_n(z_i) = 0$ . The  $n - 1$  intervals between adjacent nodes, denoted as  $\{d_i\}_{i=1}^{n-1}$  and defined by  $d_i \equiv z_{i+1} - z_i$ , are termed nodal distances. For

<sup>1</sup>The existence of non-spherical solutions of the stationary Schrödinger-Poisson system (4) is still an unsolved problem (see Hui et al. [2], Appendix B).



(a) Structure of the eigenfunction showing nodes and extrema.



(b) Detailed view with notation.

Figure 2: Structure and notation of eigenfunction  $f_8(r)$ . Panel (a) shows the complete eigenfunction, with nodes  $\{z_i\}_{i=1}^8$  marked in orange and local extrema  $\{(\hat{r}_i, \hat{f}_i)\}_{i=0}^8$  in green. Panel (b) provides a magnified view highlighting the notation, including the first two nodal distances  $\{d_i\}_{i=1}^7$  with  $d_i \equiv z_{i+1} - z_i$ .

each distance  $d_i$ , we refer to  $z_{i+1}$  and  $z_i$  as the right and left nodes, respectively.

The  $n + 1$  local extrema, denoted by  $\{(\hat{r}_i, \hat{f}_i)\}_{i=0}^n$ , alternate in sign and decrease in amplitude. The central point  $(\hat{r}_0, \hat{f}_0)$  represents the global maximum of the eigenfunction, while the outermost local extremum  $(\hat{r}_n, \hat{f}_n)$  marks the end of the oscillating region, beyond which the eigenfunction decreases monotonically to zero. In physical applications, the radius  $\hat{r}_n$  serves as an indicator of the function's effective support.

When applying these eigenstates to model galactic dark matter clusters, the squared modulus  $|f_n|^2(r)$  represents the dark matter density distribution. Its three-dimensional structure, revealed through the simulations and shown in Figure 1, describes dark matter as arranged in concentric spherical shells of decreasing density. The quantitative study that follows characterizes this structure by deriving precise heuristic laws, that describe its dependence on the excitation index  $n$ .

### 3.2. Approximate support

Let us examine the radial position  $\hat{r}_n(n)$  of the outermost local extremum, which serves as an indicator of the function's support in physical applications. We computed its value for several excitation indices  $n$ , with the results displayed in Figure 3. The data reveals a clear parabolic relationship, resulting in the following numerical fit:

$$\hat{r}_n(n) = 131n^2 + 53.53n + 340. \quad (5)$$

This heuristic law provides valuable physical insight by describing how the effective support of the matter distribution  $f_n^2(r)$  varies with the excitation index  $n$ . Note that the asymptotic scaling  $\hat{r}_n(n) \sim n^2$ , observed at large  $n$  is characteristic of the quantum Keplerian or hydrogenoid problems (see Griffiths [22]).

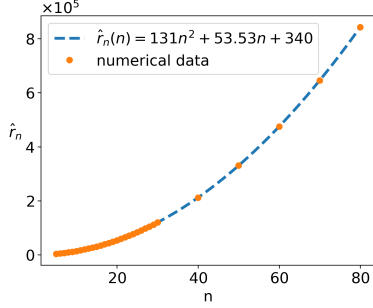


Figure 3: Parabolic fit for the radial position  $\hat{r}_n(n)$  of the outermost local extremum, serving as an indicator of the function's support.

### 3.3. Nodal distances

Let us then examine the nodal distances  $\{d_i\}_{i=1}^{n-1}$  between adjacent nodes. As Figure 2 suggests, these distances appear to increase with radial position. To investigate this observation further, Figure 4 reports the nodal distances  $\{d_i\}_{i=1}^{n-1}$  against their corresponding right nodes  $\{z_{i+1}\}_{i=1}^{n-1}$ , where we recall  $d_i \equiv z_{i+1} - z_i$ . The plot includes several sample eigenfunctions  $f_n(r)$  to illustrate the behavior across different excitation indices  $n$ .

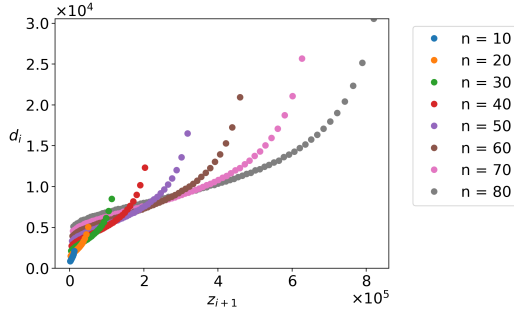


Figure 4: Nodal distances  $\{d_i\}_{i=1}^{n-1}$  plotted against their corresponding right nodes  $\{z_{i+1}\}_{i=1}^{n-1}$ , for several sample eigenfunctions.

The figure confirms that, for each eigenfunction  $f_n(r)$ , the nodal distances  $\{d_i\}_{i=1}^{n-1}$  increase with radial position, showing modest growth for the initial nodes but substantial increases for the final nodes. Moreover, this pattern remains consistent across different eigenfunctions, exhibiting similar behavior as the excitation index  $n$  varies.

To examine the regularity of this nodal distance pattern, we seek an appropriate rescaling of the curves in Figure 4 that might reveal a common underlying structure across different values of  $n$ . A natural approach is to normalize the patterns using their outermost point  $(z_n, d_{n-1})$ , which comprises the outer-

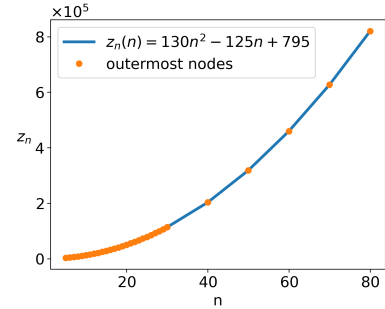
most node  $z_n$  and the outermost nodal distance  $d_{n-1} \equiv z_n - z_{n-1}$ :

$$Z_{i+1} \equiv \frac{z_{i+1}}{z_n(n)}; \quad D_i \equiv \frac{d_i}{d_{n-1}(n)}; \quad \text{for } i = 1, \dots, n-1. \quad (6)$$

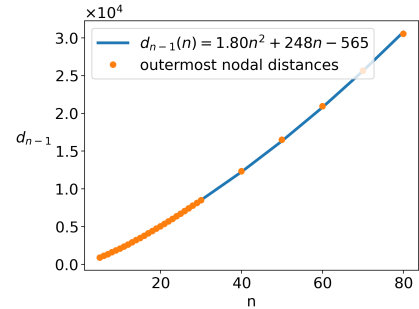
For this rescaling to be meaningful and truly capture the fundamental pattern structure, we expect the scaling quantities to exhibit a clear dependence on the excitation index,  $z_n(n)$  and  $d_{n-1}(n)$ . Testing this hypothesis in Figure 5, we find that both quantities follow a distinct parabolic relationship with  $n$ , which can be quantitatively expressed as:

$$z_n(n) = 130n^2 - 125n + 795; \quad (7a)$$

$$d_{n-1}(n) = 1.80n^2 + 248n - 565. \quad (7b)$$



(a) Parabolic fit of the outermost node  $z_n(n)$ .



(b) Parabolic fit of the outermost nodal distance  $d_{n-1}(n)$ .

Figure 5: Variation with excitation index  $n$  of (a) the outermost node  $z_n(n)$  and (b) the outermost nodal distance  $d_{n-1}(n)$  of the eigenfunction.

The heuristic laws (7) validate our choice of the outermost point  $(z_n(n), d_{n-1}(n))$  for characterizing the nodal distance pattern. Since this point depends solely on the excitation index, it captures a fundamental property of the eigenfunction and provides an effective basis for the rescaling defined in Equations (6).

As shown in Figure 6, the rescaled nodal distance patterns, while not perfectly coincident, demonstrate increasing convergence with larger values of  $n$ , approaching a universal curve in the large  $n$  limit.

### 3.4. Amplitude modulation

Let us now examine the eigenfunction's local extrema  $\{(\hat{r}_i, \hat{f}_i)\}_{i=0}^n$ , whose amplitudes  $|\hat{f}_i|$  decrease with increasing  $\hat{r}_i$ .

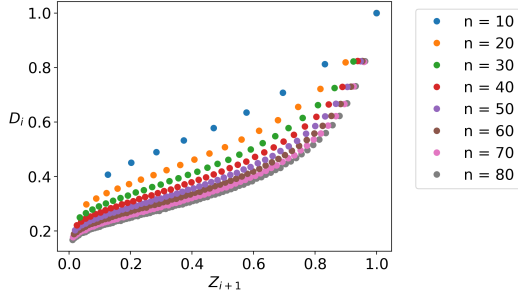


Figure 6: Normalized nodal distances  $\{D_i\}_{i=1}^{n-1}$  plotted against their normalized right nodes  $\{Z_{i+1}\}_{i=1}^{n-1}$ , for several sample eigenfunctions. Normalization follows Equation (6).

To formalize this behavior, in Figure 7 we present a logarithmic scale plot of the absolute values of local extrema  $\{(\hat{r}_i, |\hat{f}_i|)\}_{i=1}^n$  for sample eigenfunctions, excluding the central extremum  $(\hat{r}_0, |\hat{f}_0|)$  since its radius  $\hat{r}_0 = 0$  is incompatible with logarithmic scaling. We observe that the inner amplitudes exhibit linear decay, while the outer amplitudes deviate from this behavior, reaching a minimum at a given  $r_{min}$  and then increasing again. Based on this, we perform a fit over the region from the first local extremum  $\hat{r}_1$  to a fixed distance before the minimum,  $0.95r_{min}$ . It results that the amplitudes follow a power law, with parameters  $a(n)$ ,  $b(n)$  dependent on the excitation index  $n$  and with negative exponent  $a(n) < 0$ :

$$|\hat{f}_i| = b(n) \hat{r}_i^{a(n)}. \quad (8)$$

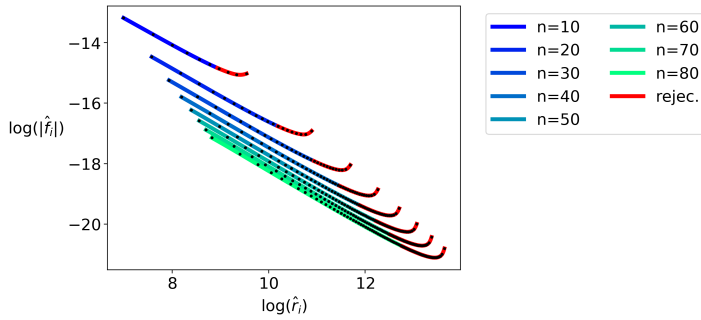


Figure 7: Logarithmic plot showing the fitted amplitudes  $\{(\hat{r}_i, |\hat{f}_i|)\}_{i=1}^n$  of eigenfunction oscillations for sample excitation indices  $n$ . Red regions indicate points deviating from linear behavior, which are excluded from the fit.

Figure 8 shows that the exponent  $a(n)$  approximately follows a power law in  $n$ , approaching the asymptotic value  $-1$  in the large  $n$  limit. The behavior stabilizes for  $n \gtrsim 20$ , which is therefore selected as the onset of the fitting region. The resulting heuristic law reads:

$$a(n) = -1 + 0.24n^{-0.25}. \quad (9a)$$

Observe that the asymptotic value  $a \sim -1$  aligns with the approximate behavior  $f_n(r) \sim r^{-1}$  commonly adopted in the literature ([1, 17]) and consistent with the flat plateau of the observed rotation curves.

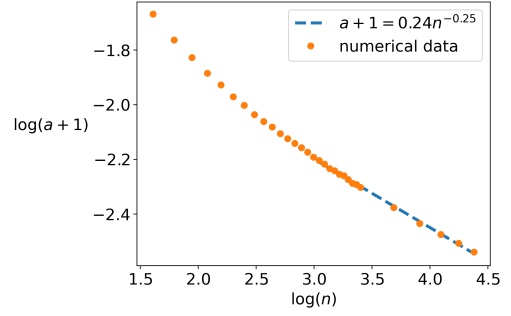
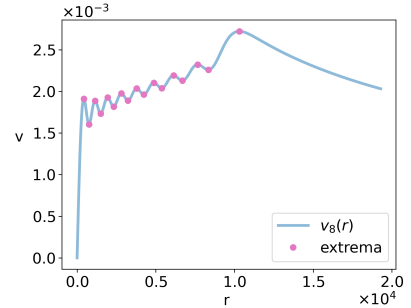


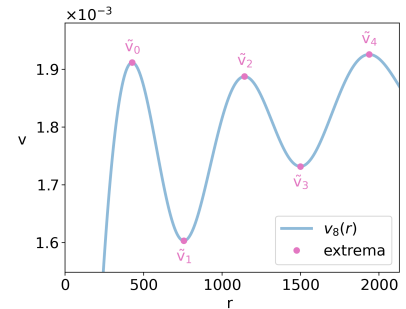
Figure 8: Power law fits for the exponential parameter  $a(n) = -1 + 0.24n^{-0.25}$ , in logarithmic scale.

### 3.5. Eigenvelocities

Finally, let us examine the eigenvelocities  $v_n(r)$  associated with the eigenfunctions  $f_n(r)$ , according to definition (2). Figure 9 presents an example, again using a low excitation index  $n = 8$  for clarity, highlighting the curve's key features.



(a) Eigenvelocity profile with extrema.



(b) Magnified view with notation.

Figure 9: Eigenvelocity  $v_n(r)$  with detailed notation. Panel (a) shows the complete eigenvelocity profile, with local extrema  $\{(\tilde{r}_i, \tilde{v}_i)\}_{i=0}^{2n}$ . Panel (b) provides a magnified view highlighting the notation.

Similarly to their experimental counterparts, namely the galactic rotation curves, these profiles exhibit three distinct regions: an initial linear raise, a mid-range oscillatory region, and a final Keplerian decline. The oscillatory region contains  $2n + 1$  local extrema, denoted by  $\{\tilde{r}_i, \tilde{v}_i\}_{i=0}^{2n}$  (see Figure 9). The radial positions  $\{\tilde{r}_i\}_{i=0}^{2n}$  of these extrema lie between the eigenfunction's nodes  $\{z_i\}_{i=1}^n$  and the eigenfunction's local extrema  $\{\hat{r}_i\}_{i=0}^n$ .

As shown in Figure 10 for sample eigenvelocities  $v_n(r)$ , the oscillating region exhibits a distinctly linear average trend. We

perform linear fits in the mid-range region, excluding the first two and last two local extrema for improved accuracy:

$$v_n(r) = \sigma(n)r + q(n) \quad \text{for } \tilde{r}_2 \leq r \leq \tilde{r}_{2n-2} \quad (10)$$

Figure 11 plots the resulting slopes  $\sigma(n)$  against the excitation number  $n$ . These slopes decrease with increasing excitation numbers, according to a power law:

$$\sigma(n) = (2.82 \cdot 10^{-5})n^{-2.86} \quad (11)$$

In the large  $n$  limit the slopes approach zero, consistent with the experimental observations of flat plateaux.

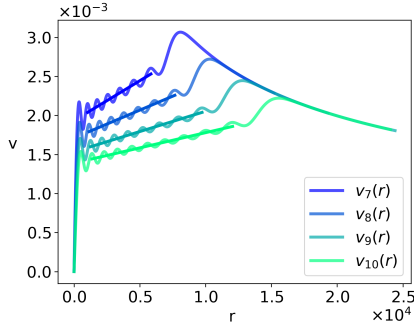


Figure 10: Examples of eigenvelocity profiles  $v_n(r)$  with mid-range linear fit.

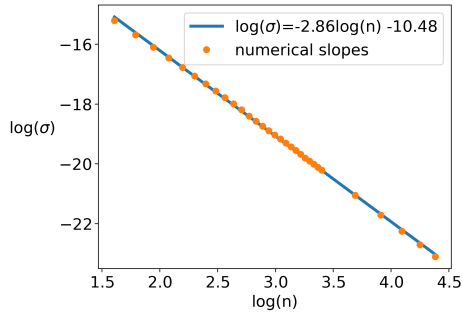


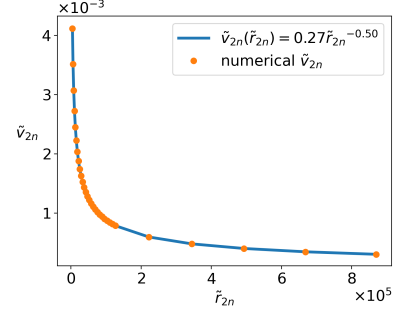
Figure 11: Power law relationship between the slopes  $\sigma(n)$  and the excitation index  $n$ , derived from mid-range fits of eigenvelocities (see Eq. 10).

To conclude, we analyze the outermost local extremum  $(\tilde{r}_{2n}, \tilde{v}_{2n})$  of the eigenvelocities. Figure 10 indicates that its velocity exhibits a clear relationship with the corresponding radius,  $\tilde{v}_{2n}(\tilde{r}_{2n})$ , while the radius shows a distinct dependence on the excitation index,  $\tilde{r}_{2n}(n)$ . These relationships, plotted in Figure 12, yield the following quantitative heuristic laws:

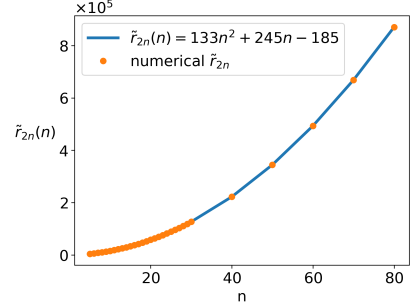
$$\tilde{v}_{2n}(\tilde{r}_{2n}) = 0.27 \tilde{r}_{2n}^{-0.5}; \quad (12a)$$

$$\tilde{r}_{2n}(n) = 133n^2 + 245n - 185. \quad (12b)$$

The radius  $\tilde{r}_{2n}(n)$  exhibits a parabolic dependence on  $n$ , similar to the behavior observed for  $\hat{r}_n(n)$  and  $z_n(n)$  in the eigenfunction. According to formula (12a), the velocity  $\tilde{v}_{2n}(\tilde{r}_{2n})$  decays as the square root of the inverse radius, consistent with a Keplerian decline encompassing the entire mass distribution.



(a) Power law fit for  $\tilde{v}_{2n}(\tilde{r}_{2n})$ .



(b) Parabolic fit for  $\tilde{r}_{2n}(n)$ .

Figure 12: Heuristic laws describing the outermost local extremum  $(\tilde{r}_{2n}(n), \tilde{v}_{2n}(\tilde{r}_{2n}))$  of the eigenvelocity  $v_n(r)$ . The velocity follows a power law in the radius (see Eq. (12a)), while the radius shows parabolic dependence on the excitation index (see Eq. (12b)).

Overall, the heuristic laws (12) suggest a natural scaling for the eigenvelocities, that depends solely on the excitation index  $n$ :

$$R \equiv \frac{r}{\tilde{r}_{2n}(n)}; \quad V \equiv \frac{v}{\tilde{v}_{2n}(n)}, \quad (13)$$

where  $\tilde{v}_{2n}(n)$  is obtained by combining Equations (12a) and (12b),  $\tilde{v}_{2n}(n) \equiv \tilde{v}_{2n}(\tilde{r}_{2n}(n))$ . Figure 13 reports eigenvelocities rescaled according to Equation (13). The plot shows how the simulated rotation curves, originally shown in Figure 10, collapse onto a single average curve after rescaling, revealing a universal behavior. This finding aligns well with physical expectations (see e.g. Rubin et al. [25], Burstein and Rubin [26]), which typically predict common underlying features in rotation curves across different galaxies.

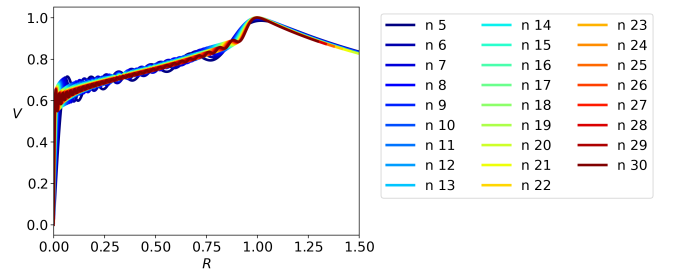


Figure 13: Universality in eigenvelocity profiles, after rescaling according to Equations (13).



## 4. Discussion and Conclusions

This work provides a characterization of excited Schrödinger-Poisson eigenstates, extending current knowledge of their fundamental properties, with particular emphasis on their agreement with physical expectations for galactic rotation curves. The analysis is based on numerically derived heuristic laws, that describe how key properties of the eigenstates scale with the excitation index  $n$ .

The eigenfunctions are characterized by two main components: oscillatory behavior and amplitude modulation. Unlike standard oscillatory functions, the nodal spacing increases with radial position, showing more pronounced growth at larger radii. The amplitudes decay following a power law, with deviations observed only at the last local extrema, and an exponent approaching  $-1$  in the large  $n$  limit. This description both aligns with and refines the widely used approximation  $f_n(r) \sim \sin(r)r^{-1}$ . The heuristic laws also provide insight into the extent of dark matter distributions, with a support – approximately defined by the radial position of the last local extremum – showing a parabolic dependence on  $n$ .

The resulting eigenvelocity characterization aligns well with physical expectations: the mid-range oscillatory region exhibits a linear trend with a positive slope, that approaches zero in the large  $n$  limit. The clear dependence on  $n$  displayed by the radial position and velocity of the last extremum provide natural scaling laws, through which a universal behavior emerges for the eigenvelocities. This universality agrees with the physical expectation of common underlying properties in dark matter distributions across different galaxies.

A natural extension of this study would be the direct comparison between model predictions and observational data, which, however, requires incorporating the baryonic component into the model (see Ji and Sin [6]). A systematic investigation of this aspect is reserved for future work.

## Acknowledgements

We thank Massimo Robberto, Lead of NIRCam STScI & Johns Hopkins University, for valuable discussions on dark matter during his visit to our Department.

We acknowledge GNFM (INdAM), the Italian national group for Mathematical Physics.

We acknowledge ICSC – Centro Nazionale di Ricerca in High Performance Computing, Big Data and Quantum Computing, funded by European Union – NextGenerationEU.

## References

[1] T. Matos, L. A. Ureña-López, J.-W. Lee, Short review of the main achievements of the scalar field, fuzzy, ultralight, wave, BEC dark matter model, *Frontiers in Astronomy and Space Sciences* 11 (2024). URL: <https://www.frontiersin.org/journals/astronomy-and-space-sciences/articles/10.3389/fspas.2024.1347518>. doi:10.3389/fspas.2024.1347518.

[2] L. Hui, J. P. Ostriker, S. Tremaine, E. Witten, Ultralight scalars as cosmological dark matter, *Phys. Rev. D* 95 (2017) 043541. URL: <https://link.aps.org/doi/10.1103/PhysRevD.95.043541>. doi:10.1103/PhysRevD.95.043541.

[3] R. Ruffini, S. Bonazzola, Systems of self-gravitating particles in general relativity and the concept of an equation of state, *Phys. Rev.* 187 (1969) 1767–1783. URL: <https://link.aps.org/doi/10.1103/PhysRev.187.1767>. doi:10.1103/PhysRev.187.1767.

[4] M. Baldeschi, G. Gelmini, R. Ruffini, On massive fermions and bosons in galactic halos, *Physics Letters B* 122 (1983) 221–224. URL: <https://www.sciencedirect.com/science/article/pii/0370269383906883>. doi:[https://doi.org/10.1016/0370-2693\(83\)90688-3](https://doi.org/10.1016/0370-2693(83)90688-3).

[5] S.-J. Sin, Late-time phase transition and the galactic halo as a Bose liquid, *Phys. Rev. D* 50 (1994) 3650–3654. URL: <https://link.aps.org/doi/10.1103/PhysRevD.50.3650>. doi:10.1103/PhysRevD.50.3650.

[6] S. U. Ji, S. J. Sin, Late-time phase transition and the galactic halo as a Bose liquid. II. The effect of visible matter, *Physical Review D* 50 (1994). URL: <https://journals.aps.org/prd/abstract/10.1103/PhysRevD.50.3655>. doi:10.1103/PhysRevD.50.3655.

[7] P. Lions, The Choquard equation and related questions, *Nonlinear Analysis: Theory, Methods & Applications* 4 (1980) 1063–1072. URL: <https://www.sciencedirect.com/science/article/pii/0362546X80900164>. doi:[https://doi.org/10.1016/0362-546X\(80\)90016-4](https://doi.org/10.1016/0362-546X(80)90016-4).

[8] F. Lelli, S. S. McGaugh, J. M. Schombert, SPARC: mass models for 175 disk galaxies with Spitzer photometry and accurate rotation curves, *The Astronomical Journal* 152 (2016) 157. URL: <https://dx.doi.org/10.3847/0004-6256/152/6/157>. doi:10.3847/0004-6256/152/6/157.

[9] H. Katz, F. Lelli, S. S. McGaugh, A. Di Cintio, C. B. Brook, J. M. Schombert, Testing feedback-modified dark matter haloes with galaxy rotation curves: estimation of halo parameters and consistency with  $\Lambda$ cdm scaling relations, *Monthly Notices of the Royal Astronomical Society* 466 (2016) 1648–1668. URL: <https://doi.org/10.1093/mnras/stw3101>. doi:10.1093/mnras/stw3101.

[10] T. Harko, E. J. Madarassy, Bose-Einstein Condensate dark matter models in the presence of baryonic matter and random confining potentials, *The European Physical Journal C* 82 (2022). URL: <http://arxiv.org/abs/2205.00297http://dx.doi.org/10.1140/epjc/s10052-022-10344-7>. doi:10.1140/epjc/s10052-022-10344-7.

[11] F. S. Guzmán, F. D. Lora-Clavijo, Rotation curves of ultralight BEC dark matter halos with rotation, *General Relativity and Gravitation* 47 (2015) 21. URL: <https://link.springer.com/article/10.1007/s10714-015-1865-9>. doi:10.1007/s10714-015-1865-9.

[12] J. Binney, S. Tremaine, *Galactic Dynamics: Second Edition*, Princeton Series in Astrophysics, Princeton University Press, 2011. URL: <https://books.google.it/books?id=6mF4CKx1bLsC>.

[13] E. H. Lieb, Existence and uniqueness of the minimizing solution of Choquard’s nonlinear equation, *Studies in Applied Mathematics* 57 (1977) 93–105. URL: <https://onlinelibrary.wiley.com/doi/abs/10.1002/sapm197757293>. doi:<https://doi.org/10.1002/sapm197757293>.

[14] D. Bernstein, E. Gilardi, K. Jones, Eigenstates of the gravitational Schrödinger equation, *Modern Physics Letters A* 13 (1998) 2327–2336. URL: <https://doi.org/10.1142/S0217732398002473>. doi:10.1142/S0217732398002473.

[15] I. M. Moroz, R. Penrose, P. Tod, Spherically-symmetric solutions of the Schrödinger-Newton equations, *Classical and Quantum Gravity* 15 (1998) 2733. URL: <https://dx.doi.org/10.1088/0264-9381/15/9/019>. doi:10.1088/0264-9381/15/9/019.

[16] R. Harrison, I. Moroz, K. P. Tod, A numerical study of the Schrödinger-Newton equations, *Nonlinearity* 16 (2002) 101. URL: <https://dx.doi.org/10.1088/0951-7715/16/1/307>. doi:10.1088/0951-7715/16/1/307.

[17] C. G. Böhrer, T. Harko, Can dark matter be a Bose-Einstein condensate?, *Journal of Cosmology and Astroparticle Physics* 2007 (2007) 025. URL: <https://dx.doi.org/10.1088/1475-7516/2007/06/025>. doi:10.1088/1475-7516/2007/06/025.

[18] P. Tod, I. M. Moroz, An analytical approach to the Schrödinger-Newton equations, *Nonlinearity* 12 (1999) 201. URL: <https://dx.doi.org/10.1088/0951-7715/12/2/002>. doi:10.1088/0951-7715/12/2/002.

- [19] K. Tod, The ground state energy of the Schrödinger-Newton equation, *Physics Letters A* 280 (2001) 173–176. URL: <https://www.sciencedirect.com/science/article/pii/S0375960101000597>. doi:[https://doi.org/10.1016/S0375-9601\(01\)00059-7](https://doi.org/10.1016/S0375-9601(01)00059-7).
- [20] D. Greiner, G. Wunner, Quantum defect analysis of the eigenvalue spectrum of the Newton-Schrödinger equation, *Phys. Rev. A* 74 (2006) 052106. URL: <https://link.aps.org/doi/10.1103/PhysRevA.74.052106>. doi:10.1103/PhysRevA.74.052106.
- [21] M. K. Kiessling, On the asymptotic decay of the Schrödinger-Newton ground state, *Physics Letters A* 395 (2021) 127209. URL: <https://www.sciencedirect.com/science/article/pii/S0375960121000736>. doi:<https://doi.org/10.1016/j.physleta.2021.127209>.
- [22] D. Griffiths, *Introduction to Quantum Mechanics*, Cambridge University Press, 2017. URL: <https://books.google.it/books?id=0h-nDAAAQBAJ>.
- [23] V. C. Rubin, J. Ford, W. K., N. Thonnard, Rotational properties of 21 SC galaxies with a large range of luminosities and radii, from NGC 4605 (R=4kpc) to UGC 2885 (R=122kpc)., *Astrophysical Journal* 238 (1980) 471–487. doi:10.1086/158003.
- [24] Y. Sofue, Rotation curve decomposition for size–mass relations of bulge, disk, and dark halo components in spiral galaxies, *Publications of the Astronomical Society of Japan* 68 (2015) 2. URL: <https://doi.org/10.1093/pasj/psv103>. doi:10.1093/pasj/psv103.
- [25] V. C. Rubin, D. Burstein, W. K. Ford, Jr., N. Thonnard, Rotation velocities of 16 SA galaxies and a comparison of Sa, Sb, and SC rotation properties, *Astrophys. J.* 289 (1985) 81. doi:10.1086/162866.
- [26] D. Burstein, V. C. Rubin, The distribution of mass in spiral galaxies., *Astrophysical Journal* 297 (1985) 423–435. doi:10.1086/163541.